J Eng Math (2009) 65:273–290
DOI 10.1007/s10665-009-9288-9

The Rayleigh–Taylor instability for inviscid and viscous fluids

Lawrence K. Forbes

Received: 8 June 2008 / Accepted: 9 March 2009 / Published online: 22 March 2009

Abstract The classical Rayleigh–Taylor instability occurs when two inviscid fluids, with a sharp interface separating them, lie in two horizontal layers with the heavier fluid above the lighter one. A small sinusoidal disturbance on the interface grows rapidly in time in this unstable situation, as the heavier upper fluid begins to move downwards through the lighter lower fluid. This paper presents a novel numerical method for computing the growth of the interface. The technique is based on a spectral representation of the solution. The results are accurate right up to the time when a curvature singularity forms at the interface and the inviscid model loses its validity. A spectral method is then presented to study the same instability in a viscous Boussinesq fluid. The results are shown to agree closely with the inviscid calculations for small to moderate times. However, the high interface curvatures that develop in the inviscid model are prevented from occurring in viscous fluid by the growth of regions of high vorticity at precisely these singular points. This leads to over-turning of the interface, to form mushroom-shaped profiles. It is shown that different initial interface configurations can lead to very different geometrical outcomes, as a result of the flow instability. These can include situations when detached bubbles form in the fluid.

Keywords Boussinesq approximation · Curvature singularity · Spectral methods · Surface roll-up · Vorticity

1 Introduction

When a horizontal layer of heavy fluid lies above another such layer of lighter fluid, the interface between them is unstable to small disturbances, which then grow as time progresses. The behaviour of an initially sinusoidal disturbance at the interface was first studied by Lord Rayleigh [1] and later by Sir Taylor [2]. In that small-amplitude analysis, the sinusoidal perturbations were shown to grow exponentially with time.

The Rayleigh–Taylor instability has since been the subject of a great deal of investigation, and there are major review articles on the topic by Sharp [3], Kull [4] and Inogamov [5]. The phenomenon occurs in a wide variety of situations and length scales. It is a feature of over-turning in the deep ocean, where mixing occurs as a result of the formation of vertical plumes, as described by Lazier et al. [6]. It is also believed to be the cause of some elaborate structures at galactic length scales, reported in the radio-telescope observations of McClure-Griffiths et al. [7].

L. K. Forbes (✉)
School of Mathematics and Physics, University of Tasmania, Private Bag 37, Hobart, TAS, Australia
e-mail: Larry.Forbes@utas.edu.au

The original analysis of Taylor [2] was based on small-amplitude theory, and, as it predicts exponential growth of the original disturbance, it must cease to be valid after some time. Nonlinear effects must be taken into account as larger amplitudes structures begin to form. Solutions of these problems then require the use of numerical methods. For the purely inviscid problem, Sharp [3] points out that numerical methods can often break down, for reasons that are poorly understood. It is now known, however, that singularities can form in finite time on the interface, for inviscid fluids. The seminal work on this problem was undertaken by Moore [8], who gave an asymptotic estimate of the critical time at which the curvature along the interface becomes infinite, for Kelvin–Helmholtz shear instability at the interface between two fluids moving at different speeds. That work has been generalized to some extent by Cowley, Baker and Tanveer [9]. They analytically continued Moore's analysis into the complex plane of the time variable t, and showed asymptotically that singularities can form spontaneously in the complex plane at early times, and then move to intersect the real t-axis, producing the curvature singularity of Moore [8].

It has been understood for some time that the curvature singularity formed at the interface between inviscid fluids may trigger over-turning and roll-up when viscous effects are included. Krasny [10] introduced a "vortex blob" method that effectively smudged the interface over a finite region, and showed that, for the Kelvin–Helmholtz instability, numerical results could be computed beyond the critical time of inviscid singularity formation. The interface over-turned and rolled up into a double spiral, so producing the familiar "cat's eyes" seen in that form of fluid instability. More recently, Baker and Pham [11] have undertaken a more systematic study of vortex blob methods, and have shown that different forms of these techniques can affect the way in which the instability develops. Tryggvason et al. [12] also considered the effect of Krasny's vortex-blob approach to the inviscid problem, and compared the results with those produced by a finite-difference solution to the Navier–Stokes equations of viscous flow. They observed reasonable similarities between the two approaches, although it is perhaps unclear to what extent this was influenced by the approach to the vortex-blob technique used. There is now a very large literature on vortex-sheet roll-up, and numerical simulations for complex geometry even in three dimensions have been undertaken for the Rayleigh–Taylor instability by Tryggvason and Unverdi [13], for example, and for the magnetohydrodynamical version of the problem by Stone and Gardiner [14].

The purpose of the present paper is to examine in detail the relationship between the inviscid model of Rayleigh–Taylor instability and its viscous counterpart. The inviscid results are obtained using a novel spectral solution technique, introduced by Forbes et al. [15] and applied subsequently to a problem involving the draining of a tank by Forbes and Hocking [16]. This technique does not rely on regularization approaches such as used in vortex-blob methods, and, is able to give accurate solutions almost up to the time at which the curvature singularity forms at the interface. A separate spectral method is then presented for the solution of the viscous flow problem in a Boussinesq fluid, and the results are found to agree very closely with the corresponding inviscid solutions. This confirms the suggestion by Farrow and Hocking [17] that viscosity plays only a minor role in the behaviour while inviscid solutions are possible, but it also indicates clearly that a viscous fluid generates small regions of high vorticity at exactly the points on the interface at which the inviscid model would produce curvature singularities. This gives a strong demonstration that the curvature singularity is indeed the trigger for roll-up in the viscous case.

2 The classical Rayleigh–Taylor model

For the classical two-dimensional Rayleigh–Taylor instability of Lord Rayleigh [1] and Taylor [2], two inviscid fluids of infinite depth are separated by a horizontal sharp interface. The upper and lower fluids are denoted as layers 2 and 1, respectively, following the notation of Batchelor [18, p. 69]. The upper fluid has density ρ_2 and the lower fluid has density ρ_1, and since the upper fluid is heavier, it follows that $\rho_2 > \rho_1$. The location of the interface is represented mathematically by the equation $y = \eta(x, t)$.

Each fluid is inviscid and incompressible and so flows irrotationally. As a result, velocity potentials ϕ_2 and ϕ_1 may be constructed in fluids 2 and 1, respectively, and horizontal and vertical fluid velocity components may be obtained according to the relationships $(u_j, v_j) = (\partial\phi_j/\partial x, \partial\phi_j/\partial y)$ in each fluid, $j = 1, 2$. Each velocity potential must satisfy Laplace's equation, so that

$$\nabla^2\phi_1 = 0 \quad \text{in } y < \eta(x,t),$$
$$\nabla^2\phi_2 = 0 \quad \text{in } y > \eta(x,t). \tag{1}$$

By definition, neither fluid is able to cross the interface, and this geometrical constraint leads to the two kinematic conditions

$$v_j = \frac{\partial \eta}{\partial t} + u_j \frac{\partial \eta}{\partial x}, \quad j = 1,2 \quad \text{on } y = \eta(x,t). \tag{2}$$

The two fluids are both subject to a downward body force per unit mass g, which may be thought of as the acceleration of gravity. In addition, the entire fluid system is accelerating vertically with acceleration a. As both fluids are inviscid, it is possible to integrate the equations of motion, so that a separate Bernoulli equation,

$$\frac{\partial \phi_j}{\partial t} + \frac{1}{2}\left(u_j^2 + v_j^2\right) + \frac{p_j}{\rho_j} + (g-a)\, y = a^2 t^2 + \frac{1}{2}(g-a)\, a t^2, \quad j = 1,2,$$

exists in each fluid. The dynamical condition that the fluid pressures p_1 and p_2 must be equal at the interface $y = \eta$ then yields the further requirement

$$\rho_2 \frac{\partial \phi_2}{\partial t} - \rho_1 \frac{\partial \phi_1}{\partial t} + \frac{1}{2}\rho_2\left(u_2^2 + v_2^2\right) - \frac{1}{2}\rho_1\left(u_1^2 + v_1^2\right) + (\rho_2 - \rho_1)(g-a)\,\eta$$
$$= \frac{1}{2}(\rho_2 - \rho_1)(g+a)\, a t^2 \quad \text{on } y = \eta(x,t). \tag{3}$$

Far above and below the interface, the vertical components v_2 and v_1 of the fluid velocity vector equal at, corresponding to uniform acceleration there.

In the classical Rayleigh–Taylor problem, small waves of wavelength λ are introduced at the interface, and these grow in time as a consequence of the inherent instability of the fluid configuration. Here, we now introduce non-dimensional coordinates and variables, using the characteristic length $\lambda/2\pi$ and time $\sqrt{\lambda/(2\pi g)}$. The appropriate scale for speed is the quantity $\sqrt{g\lambda/(2\pi)}$. In this new dimensionless formulation, there are thus two parameters

$$D = \rho_2/\rho_1 \qquad \alpha = a/g \tag{4}$$

that define the state of the system. The first of these non-dimensional quantities is the density ratio, and we are concerned with the unstable situation $D > 1$. The second is the ratio of the fluid acceleration to the body force per mass experienced by the two fluids. The dimensionless problem thus has period 2π in the x-coordinate, as illustrated in Fig. 1.

In these dimensionless coordinates, the two velocity potentials continue to obey the Laplace equations (1) and the two kinematic conditions (2) on the interface. Far away, the conditions

$$u_1 \to 0, \quad v_1 \to \alpha t \quad \text{as } y \to -\infty,$$
$$u_2 \to 0, \quad v_2 \to \alpha t \quad \text{as } y \to \infty \tag{5}$$

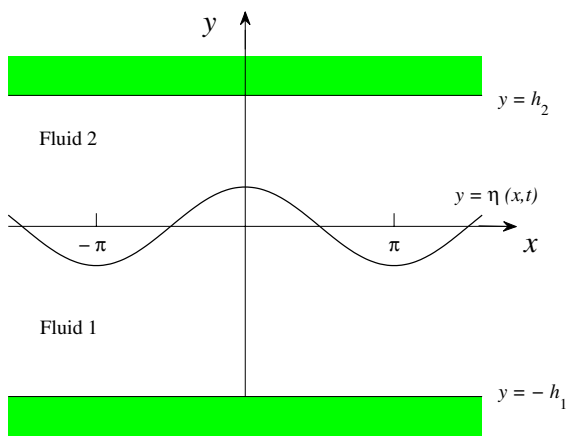

Fig. 1 A sketch of the dimensionless flow configuration for the inviscid Rayleigh–Taylor problem with zero acceleration and finite fluid depths

express the fact that the flow occurs with uniform acceleration α. The dynamical condition (3) now becomes

$$D\frac{\partial\phi_2}{\partial t} - \frac{\partial\phi_1}{\partial t} + \frac{1}{2}D\left(u_2^2+v_2^2\right) - \frac{1}{2}\left(u_1^2+v_1^2\right) + (D-1)(1-\alpha)\eta$$
$$= \frac{1}{2}(D-1)(1+\alpha)\alpha t^2 \quad \text{on } y=\eta(x,t) \tag{6}$$

in non-dimensional form.

It is convenient at this point to define perturbed velocity potentials Φ_1 and Φ_2 and interface height H by means of the relations

$$\phi_1(x,y,t) = \alpha t y + \Phi_1(x,y,t)$$
$$\phi_2(x,y,t) = \alpha t y + \Phi_2(x,y,t)$$
$$\eta(x,t) = \frac{1}{2}\alpha t^2 + H(x,t). \tag{7}$$

These are then substituted in the governing equations to derive a modified set, involving the new perturbed quantities. Once this is done, it is appropriate to define a new accelerating coordinate Y that moves with the fluids, by means of the equation

$$y = Y + \frac{1}{2}\alpha t^2. \tag{8}$$

In these new variables and coordinates, the Laplace equations (1) become

$$\frac{\partial^2\Phi_1}{\partial x^2} + \frac{\partial^2\Phi_1}{\partial Y^2} = 0 \quad \text{in } Y < H(x,t),$$
$$\frac{\partial^2\Phi_2}{\partial x^2} + \frac{\partial^2\Phi_2}{\partial Y^2} = 0 \quad \text{in } Y > H(x,t) \tag{9}$$

and the two kinematic conditions (2) take the form

$$\frac{\partial\Phi_j}{\partial Y} = \frac{\partial H}{\partial t} + \frac{\partial\Phi_j}{\partial x}\frac{\partial H}{\partial x}, \quad j=1,2 \quad \text{on } Y = H(x,t). \tag{10}$$

The dynamic condition (6) simplifies to become

$$D\frac{\partial\Phi_2}{\partial t} - \frac{\partial\Phi_1}{\partial t} + \frac{1}{2}D\left[\left(\frac{\partial\Phi_2}{\partial x}\right)^2 + \left(\frac{\partial\Phi_2}{\partial Y}\right)^2\right] - \frac{1}{2}\left[\left(\frac{\partial\Phi_1}{\partial x}\right)^2 + \left(\frac{\partial\Phi_1}{\partial Y}\right)^2\right] + (D-1)H = 0$$
$$\text{on } Y = H(x,t) \tag{11}$$

and the flow conditions (5) at infinity are simply

$$(\partial\Phi_1/\partial x, \partial\Phi_1/\partial Y) \to (0,0) \quad \text{as } Y \to -\infty,$$
$$(\partial\Phi_2/\partial x, \partial\Phi_2/\partial Y) \to (0,0) \quad \text{as } Y \to \infty. \tag{12}$$

The fluid acceleration parameter α now no longer appears in these governing equations (9)–(12) for the perturbed quantities in (7). It therefore does not play a major role in the evolution of the unstable flow in time.

For a small initial sinusoidal disturbance to the interface, it is straightforward to linearize the governing equations, by retaining only first-order terms in the perturbed potentials Φ_1 and Φ_2 and evaluating the linearized dynamic and kinematic boundary conditions on the undisturbed interface level $Y = 0$. This results in the famous approximate solution given by Taylor [2]. In the present notation, if it is supposed that both velocity potentials are zero at time $t = 0$ and that the interface has the initial shape $H(x,0) = \epsilon\cos x$ for some small amplitude parameter ϵ, then the linearized solution may be derived in the form

$$\Phi_1(x,Y,t) = \epsilon\sqrt{\mathcal{A}}\sinh(t\sqrt{\mathcal{A}})e^Y\cos x + \mathcal{O}(\epsilon^2),$$
$$\Phi_2(x,Y,t) = -\epsilon\sqrt{\mathcal{A}}\sinh(t\sqrt{\mathcal{A}})e^{-Y}\cos x + \mathcal{O}(\epsilon^2),$$
$$H(x,t) = \epsilon\cosh(t\sqrt{\mathcal{A}})\cos x + \mathcal{O}(\epsilon^2). \tag{13}$$

The constant

$$\mathcal{A} = \frac{D-1}{D+1}$$

is the Atwood number, and for Rayleigh–Taylor flow takes values in the interval $0 < \mathcal{A} < 1$.

Nonlinear solutions may be computed using the spectral method of Forbes et al. [15]. The appropriate forms of the two perturbed potentials that satisfy Laplace's equations (9) are

$$\begin{aligned}\Phi_1(x, Y, t) &= P_0(t) + \sum_{n=1}^{N} P_n(t) \mathrm{e}^{nY} \cos(nx),\\ \Phi_2(x, Y, t) &= Q_0(t) + \sum_{n=1}^{N} Q_n(t) \mathrm{e}^{-nY} \cos(nx),\end{aligned} \tag{14}$$

in which the time-dependent Fourier coefficients are to be determined. In fact, it is possible to set $P_0(t) = 0$ with no loss of generality, and this is assumed hereafter.

To allow for the possibility of an overhanging wave, the interface is parametrized using the Pythagorean arclength s, which is defined from the relation $\mathrm{d}s^2 = \mathrm{d}x^2 + \mathrm{d}H^2$. It is assumed that $s = 0$ at $x = 0$, but the arclength will have the unknown time-dependent values $s = \pm L(t)$ at $x = \pm\pi$. It is convenient now to introduce a new scaled arclength ξ defined as

$$\xi = \pi s / L(t). \tag{15}$$

This has the advantage that it takes known values $\xi = 0$ at $x = 0$ and $\xi = \pm\pi$ at $x = \pm\pi$. The parametric representation of the interface in terms of this new arclength (15) is therefore

$$\begin{aligned}x(\xi, t) &= \xi + \sum_{n=1}^{N} A_n(t) \sin(n\xi),\\ H(\xi, t) &= B_0(t) + \sum_{n=1}^{N} B_n(t) \cos(n\xi).\end{aligned} \tag{16}$$

The time-dependent Fourier coefficients in this expression are again to be determined, along with the interface half-length $L(t)$ in (15). The integer N in these representations (14) and (16) is the number of Fourier modes used in the approximate numerical solution and should ideally be chosen as large as possible. The use of an arclength introduces the additional equation

$$\left(\frac{\partial x}{\partial \xi}\right)^2 + \left(\frac{\partial H}{\partial \xi}\right)^2 = \frac{L^2(t)}{\pi^2} \tag{17}$$

for determining the coefficients in the representation (16).

When the equations of (16) are substituted in the arclength equation (17) and integrated over a period $-\pi < \xi < \pi$, this zeroth-order Fourier decomposition leads to the result

$$L^2(t)/\pi^2 = 1 + \frac{1}{2} \sum_{n=1}^{N} n^2 \left[A_n^2(t) + B_n^2(t)\right], \tag{18}$$

from which the unknown interface half-length $L(t)$ can be found, in terms of the other coefficients. Following Forbes et al. [15], the arclength equation (17) is now differentiated with respect to t holding ξ constant, and Fourier decomposed by multiplying by basis functions $\cos(j\xi)$ and integrating over a period. After a little algebra, this leads to a set of differential equations

$$\sum_{n=1}^{N} n\mathcal{M}_{jn} A_n'(t) - \sum_{n=1}^{N} n\mathcal{N}_{jn} B_n'(t) = 0 \quad j = 1, \ldots, N, \tag{19}$$

involving the Fourier coefficients in the parametric representation (16) of the interface. The intermediate quantities in this expression are defined to be

$$\mathcal{M}_{jn}(t) = \int_{-\pi}^{\pi} \left(\frac{\partial x}{\partial \xi}\right) \cos(n\xi)\cos(j\xi)\,\mathrm{d}\xi,$$

$$\mathcal{N}_{jn}(t) = \int_{-\pi}^{\pi} \left(\frac{\partial H}{\partial \xi}\right) \sin(n\xi)\cos(j\xi)\,\mathrm{d}\xi. \tag{20}$$

These integrals may be evaluated to high accuracy using the trapezoidal rule, which is exponentially accurate for these periodic integrands (see [19, p. 253]). In addition, each integrand is even, so that only half the domain of integration need be considered.

The kinematic conditions (10) are likewise decomposed spectrally. Firstly, it is convenient to define

$$U_1(x,t) = \frac{\partial \Phi_1}{\partial x} = -\sum_{n=1}^{N} n P_n(t) \mathrm{e}^{nH} \sin(nx),$$

$$V_1(x,t) = \frac{\partial \Phi_1}{\partial Y} = \sum_{n=1}^{N} n P_n(t) \mathrm{e}^{nH} \cos(nx),$$

$$U_2(x,t) = \frac{\partial \Phi_2}{\partial x} = -\sum_{n=1}^{N} n Q_n(t) \mathrm{e}^{-nH} \sin(nx),$$

$$V_2(x,t) = \frac{\partial \Phi_2}{\partial Y} = -\sum_{n=1}^{N} n Q_n(t) \mathrm{e}^{-nH} \cos(nx). \tag{21}$$

These are essentially perturbation velocity components in the accelerating reference frame, and will be evaluated along the interface. From the chain rule of calculus, it follows that

$$(\partial H/\partial x)_t = \frac{(\partial H/\partial \xi)_t}{(\partial x/\partial \xi)_t}, \quad (\partial H/\partial t)_x = (\partial H/\partial t)_\xi - \frac{(\partial H/\partial \xi)_t\,(\partial x/\partial t)_\xi}{(\partial x/\partial \xi)_t}. \tag{22}$$

where the subscripts denote the variables to be held constant during the differentiation. In terms of the new arc-length coordinate ξ in (15) and the perturbation velocities (21), and making use of the results (22), the two kinematic conditions (10) may be written

$$V_1 \left(\frac{\partial x}{\partial \xi}\right)_t - U_1 \left(\frac{\partial H}{\partial \xi}\right)_t = \left(\frac{\partial H}{\partial t}\right)_\xi \left(\frac{\partial x}{\partial \xi}\right)_t - \left(\frac{\partial H}{\partial \xi}\right)_t \left(\frac{\partial x}{\partial t}\right)_\xi \tag{23}$$

and

$$(V_2 - V_1)\,(\partial x/\partial \xi)_t = (U_2 - U_1)\,(\partial H/\partial \xi)_t. \tag{24}$$

This second equation is the difference of the two equations in the system (10).

To obtain the zeroth-order term in the Fourier decomposition of the first kinematic interfacial condition, Eq. 23 is integrated over a period. It is possible to make use of the identity

$$\int_{-\pi}^{\pi} V_1(x,t) \left(\frac{\partial x}{\partial \xi}\right)_t \mathrm{d}\xi = \int_{-\pi}^{\pi} U_1(x,t) \left(\frac{\partial H}{\partial \xi}\right)_t \mathrm{d}\xi,$$

which follows from the use of (21) and integration by parts. The zeroth-order term then gives

$$B_0(t) = -\frac{1}{2} \sum_{n=1}^{N} n A_n(t) B_n(t). \tag{25}$$

It is possible to use this result (25) to show that the average perturbed interface level $H(x,t)$ must remain zero for all times, and details of a similar calculation are given in Forbes et al. [15].

Higher Fourier modes in the decomposition of the first kinematic condition (24) are obtained by multiplying by basis functions $\cos(j\xi)$ and integrating over a period. Integration by parts and equations (21) give rise to the indentity

$$\int_{-\pi}^{\pi} V_1(x,t)\left(\frac{\partial x}{\partial \xi}\right)_t \cos(j\xi)\,\mathrm{d}\xi = \int_{-\pi}^{\pi} U_1(x,t)\left(\frac{\partial H}{\partial \xi}\right)_t \cos(j\xi)\,\mathrm{d}\xi + j\sum_{n=1}^{N} S_{jn}^{(1)} P_n(t),$$

from which it follows that

$$\sum_{n=1}^{N}\left[\mathcal{N}_{jn} + \frac{1}{2}jn\pi A_j(t)B_n(t)\right]A_n'(t) - \sum_{n=1}^{N}\left[\mathcal{M}_{jn} - \frac{1}{2}jn\pi A_j(t)A_n(t)\right]B_n'(t)$$
$$= -j\sum_{n=1}^{N} S_{jn}^{(1)} P_n(t), \quad j = 1,2,\ldots,N. \tag{26}$$

In this system of equations, the functions $\mathcal{M}_{jn}$ and $\mathcal{N}_{jn}$ are as defined in (20). Here, and for later use also, additional intermediate functions

$$S_{jn}^{(1)}(t) = \int_{-\pi}^{\pi} \mathrm{e}^{nH}\sin(nx)\sin(j\xi)\,\mathrm{d}\xi, \quad S_{jn}^{(2)}(t) = \int_{-\pi}^{\pi} \mathrm{e}^{-nH}\sin(nx)\sin(j\xi)\,\mathrm{d}\xi \tag{27}$$

have been defined. These may be evaluated to very high accuracy using trapezoidal-rule integration.

The second kinematic condition is now subjected to the same Fourier analysis. The zeroth mode is obtained by integrating (24) over the interval $[-\pi,\pi]$. However, the use of integration by parts and the definitions in (21) show that this zeroth mode is satisfied as an identity. The higher modes are generated by multiplying by the basis functions $\cos(j\xi)$, $j = 1,2,\ldots,N$ and integrating over a period. Integration by parts then gives rise to the elegant identity

$$\sum_{n=1}^{N} S_{jn}^{(1)} P_n(t) + \sum_{n=1}^{N} S_{jn}^{(2)} Q_n(t) = 0, \quad j = 1,2,\ldots,N \tag{28}$$

in which the two intermediate functions are as defined in (27). In order to obtain a system of ordinary differential equations for the Fourier coefficients, Eq. 28 is differentiated with respect to t, following Forbes et al. [15]. After some algebra, this leads to the system

$$-\sum_{n=1}^{N} K_{jn}A_n'(t) - \sum_{n=1}^{N} L_{jn}B_n'(t) + \sum_{n=1}^{N} S_{jn}^{(1)} P_n'(t) + \sum_{n=1}^{N} S_{jn}^{(2)} Q_n'(t) = 0, \quad j = 1,2,\ldots,N. \tag{29}$$

In these equations, the further intermediate functions

$$K_{jn}(t) = \int_{-\pi}^{\pi}\left(\frac{1}{2}nB_n(t)\left[U_2(x,t) - U_1(x,t)\right] + \sin(n\xi)\left[V_2(x,t) - V_1(x,t)\right]\right)\sin(n\xi)\,\mathrm{d}\xi,$$
$$L_{jn}(t) = \int_{-\pi}^{\pi}\left[\frac{1}{2}nA_n(t) - \cos(n\xi)\right]\left[U_2(x,t) - U_1(x,t)\right]\sin(n\xi)\,\mathrm{d}\xi \tag{30}$$

have been defined. Again, these may be evaluated to high accuracy using trapezoidal-rule quadrature, since their integrands are periodic.

Finally, the dynamic interface condition (11) is also decomposed into Fourier components. For completeness, the surface-tension term

$$\sigma\kappa = \sigma\frac{\eta_{xx}}{\left[1+\eta_x^2\right]^{3/2}}$$

is added to the left-hand side of (11). The constant σ is a dimensionless surface-tension number and κ is the curvature of the interface. The inclusion of this term is occasionally useful in regularizing the solution, as described in Forbes et al. [15], although the solutions to be presented in Sect. 5 in fact all use $\sigma = 0$. In terms of the arclength parametrization, the curvature term becomes

$$\kappa = \frac{\pi^3}{L^3(t)}\left[x_\xi H_{\xi\xi} - x_{\xi\xi} H_\xi\right], \tag{31}$$

in which $L(t)$ is the interface half-length defined in (18). The zeroth-order decomposition is achieved by integrating over a single period, and gives the result

$$2\pi D Q_0'(t) + D\sum_{n=1}^{N} C_{0n}^{(2)} Q_n'(t) - \sum_{n=1}^{N} C_{0n}^{(1)} P_n'(t) = -\frac{1}{2} D J_0^{(2)} + \frac{1}{2} J_0^{(1)} - 2\pi(D-1)B_0 - \sigma T_0. \tag{32}$$

Similarly, the higher-order modes follow after multiplication by the basis functions $\cos(j\xi)$, $j = 1, 2, \ldots, N$ and integration, giving

$$D\sum_{n=1}^{N} C_{jn}^{(2)} Q_n'(t) - \sum_{n=1}^{N} C_{jn}^{(1)} P_n'(t) = -\frac{1}{2} D J_j^{(2)} + \frac{1}{2} J_j^{(1)} - \pi(D-1)B_j - \sigma T_j, \quad j = 1, 2, \ldots, N. \tag{33}$$

These sets of equations (32), (33) have made use of the additional intermediate functions

$$\begin{aligned} C_{jn}^{(1)}(t) &= \int_{-\pi}^{\pi} e^{nH} \cos(nx)\cos(j\xi)\,\mathrm{d}\xi, \\ C_{jn}^{(2)}(t) &= \int_{-\pi}^{\pi} e^{-nH} \cos(nx)\cos(j\xi)\,\mathrm{d}\xi \quad j = 0, 1, 2, \ldots, N \end{aligned} \tag{34}$$

and

$$\begin{aligned} J_j^{(1)}(t) &= \int_{-\pi}^{\pi} \left[U_1^2(x,t) + V_1^2(x,t)\right]\cos(j\xi)\,\mathrm{d}\xi, \\ J_j^{(2)}(t) &= \int_{-\pi}^{\pi} \left[U_2^2(x,t) + V_2^2(x,t)\right]\cos(j\xi)\,\mathrm{d}\xi, \\ T_j &= \int_{-\pi}^{\pi} \kappa\cos(j\xi)\,\mathrm{d}\xi, \quad j = 0, 1, 2, \ldots, N. \end{aligned} \tag{35}$$

Equations (19), (26), (29), (32) and (33) form a coupled system of $4N + 1$ ordinary differential equations of the form

$$\mathbf{R}\frac{\mathrm{d}\mathbf{X}}{\mathrm{d}t} = \mathbf{S} \tag{36}$$

for the vector

$$\mathbf{X}(t) = [A_n(t), B_n(t), P_n(t), Q_0(t), Q_n(t)]^T$$

of Fourier coefficients. The matrix $\mathbf{R}$ and the vector $\mathbf{S}$ contain the intermediate functions defined in (20), (27), (30), (34) and (35), which are all evaluated using trapezoidal-rule quadrature. This system of differential equations is integrated forward in time using a fourth-order Runge–Kutta rule, typically using 201 mesh points over one period of the interface. With $N = 30$–50 Fourier coefficients, the method is capable of giving results of very high accuracy.

3 Inviscid Rayleigh–Taylor flows in finite depth

The system of equations (9)–(12) for the perturbed quantities showed that the fluid acceleration parameter α does not play a major role in the structure of the inviscid solution. Accordingly, we consider here the extreme in which $\alpha = 0$ and the two fluids are confined between horizontal walls at (dimensionless) locations $y = -h_1$ and $y = h_2$. There is no need here for the accelerating coordinate Y defined in (8), and the fluid motion is now purely a consequence of buoyancy effects. This flow configuration is illustrated in Fig.1. The governing equations are the same as in Sect. 2, and consist of Laplace's equations (1), the two kinematic conditions (2) and the dynamic condition (6) with $\alpha = 0$ on the interface. However, the conditions (5) are now replaced with a statement that the fluid cannot cross the upper or lower surfaces, which may be expressed in the forms

$$\begin{aligned} v_1 &= 0 \quad \text{on} \quad y = -h_1, \\ v_2 &= 0 \quad \text{on} \quad y = h_2. \end{aligned} \tag{37}$$

For small-amplitude initial disturbances, a linearized solution may be developed, and is similar to the classical result (13) given by Taylor [2]. At time $t = 0$, it is again assumed that both velocity potentials are zero and that an initial disturbance $\eta(x, 0) = \epsilon \cos x$ is made to the interface. It then follows that the solution, correct to first order in the starting amplitude ϵ, is

$$\begin{aligned} \phi_1(x, y, t) &= \epsilon r \sinh(rt) \frac{\cosh(y + h_1)}{\sinh(h_1)} \cos x + \mathcal{O}(\epsilon^2), \\ \phi_2(x, y, t) &= -\epsilon r \sinh(rt) \frac{\cosh(y - h_2)}{\sinh(h_2)} \cos x + \mathcal{O}(\epsilon^2), \\ \eta(x, t) &= \epsilon \cosh(rt) \cos x + \mathcal{O}(\epsilon^2). \end{aligned} \tag{38}$$

The constant r in these expressions is defined from the relation

$$r^2 = \frac{(D - 1) \tanh(h_1) \tanh(h_2)}{D \tanh(h_1) + \tanh(h_2)} \tag{39}$$

and gives the linearized growth rate of the instability. If $h_1, h_2 \to \infty$, so that both walls move infinitely far away from the interface, Eq. 39 shows that $r^2 \to \mathcal{A}$, which is the Atwood number in (13), as expected.

For the nonlinear solution, the appropriate representations of the two velocity potentials are

$$\begin{aligned} \phi_1(x, y, t) &= P_0(t) + \sum_{n=1}^{N} P_n(t) \cosh\left(n(y + h_1)\right) \cos(nx), \\ \phi_2(x, y, t) &= Q_0(t) + \sum_{n=1}^{N} Q_n(t) \cosh\left(n(y - h_2)\right) \cos(nx). \end{aligned} \tag{40}$$

These functions (40) satisfy Laplace's equations (1) and the bottom conditions (37).

As in Sect. 2, a nonlinear solution may be computed using the arclength formulation (15) and the same parametric representation (16) of the interface. The same arguments based on integration by parts may be used as before, and eventually, a system of $4N + 1$ differential equations may be derived for the Fourier coefficients, similar to the system (36). This is solved using a Runge–Kutta method to integrate the coefficients forward in time. Once they have been obtained, the full solution is reconstructed from (40).

4 Viscous Rayleigh–Taylor flows in finite depth

A complete understanding of Rayleigh–Taylor instability is not possible without considering the effects of viscosity, as will become apparent in Sect. 5. Rather than treat the full Navier–Stokes equations of viscous flow, with a sharp interface as in Sects. 2 and 3, we instead use the approximate Boussinesq approach adopted by Farrow and

Hocking [17]. The fluid is assumed to be weakly compressible, so that the interface can be regarded as a rapid but smooth transition from one density state to another. In dimensional variables, the density ρ is taken to have the form $\rho = \rho_0 + \bar{\rho}$, in which ρ_0 is a constant reference density and $\bar{\rho}$ is a small variation to it.

Dimensionless variables are again introduced, as in Sect. 2, using characteristic length $\lambda/2\pi$, time $\sqrt{\lambda/(2\pi g)}$ and characteristic speed $\sqrt{g\lambda/(2\pi)}$. The perturbation density $\bar{\rho}$ is made dimensionless with respect to the constant value ρ_0 and the scale for pressure is $(\rho_0 g\lambda)/(2\pi)$. Using the notation (u, v) to denote horizontal and vertical velocity components as before, we split the conservation equation for mass into an incompressible equation

$$\frac{\partial u}{\partial x} + \frac{\partial v}{\partial y} = 0 \tag{41}$$

and an equation for the transport of the perturbation density, of the form

$$\frac{\partial \bar{\rho}}{\partial t} + u\frac{\partial \bar{\rho}}{\partial x} + v\frac{\partial \bar{\rho}}{\partial y} = \gamma\left(\frac{\partial^2 \bar{\rho}}{\partial x^2} + \frac{\partial^2 \bar{\rho}}{\partial y^2}\right), \tag{42}$$

representing the weakly compressible nature of the fluid. The parameter γ is a small diffusion coefficient. The Laplace equations (1) for inviscid fluid must now be replaced by the viscous momentum equations

$$\begin{aligned}
&\frac{\partial u}{\partial t} + u\frac{\partial u}{\partial x} + v\frac{\partial u}{\partial y} + \frac{\partial p}{\partial x} = \beta\left(\frac{\partial^2 u}{\partial x^2} + \frac{\partial^2 u}{\partial y^2}\right),\\
&\frac{\partial v}{\partial t} + u\frac{\partial v}{\partial x} + v\frac{\partial v}{\partial y} + \frac{\partial p}{\partial y} = -\bar{\rho} + \beta\left(\frac{\partial^2 v}{\partial x^2} + \frac{\partial^2 v}{\partial y^2}\right).
\end{aligned} \tag{43}$$

The parameter β in these equations is the dimensionless viscosity coefficient, and may be regarded as the inverse of a Reynolds number based on wavelength.

It is convenient at this stage to introduce the stream function $\psi(x, y, t)$ through the usual definition

$$u = \frac{\partial \psi}{\partial y} \quad \text{and} \quad v = -\frac{\partial \psi}{\partial x}. \tag{44}$$

These relations (44) satisfy the incompressibility condition (41) identically. In addition, the planar vorticity ζ is defined in the usual way according to the relation

$$\zeta = \frac{\partial v}{\partial x} - \frac{\partial u}{\partial y} = -\nabla^2 \psi. \tag{45}$$

For a truly viscous fluid it would be necessary to stipulate a no-slip condition on the upper and lower horizontal walls. However, interest here is focussed on the behaviour of the fluid near the interface, and consequently, the boundary layers on the two walls are of no particular concern. We therefore follow Farrow and Hocking [17] in permitting slip conditions at the walls, expressed by the equations

$$v = \zeta = 0 \quad \text{at } y = -h_1, h_2. \tag{46}$$

By periodicity and symmetry, it is also to be expected that $u = 0$ at $x = \pm\pi$.

A spectral solution is sought to these governing equations. It is possible to eliminate the pressure p from the momentum equations (43) by differentiation and subtraction, thus giving the familiar vorticity equation

$$\frac{\partial \zeta}{\partial t} + u\frac{\partial \zeta}{\partial x} + v\frac{\partial \zeta}{\partial y} = -\frac{\partial \bar{\rho}}{\partial x} + \beta\left(\frac{\partial^2 \zeta}{\partial x^2} + \frac{\partial^2 \zeta}{\partial y^2}\right), \tag{47}$$

which may be found in [18, p. 267], for example. This vorticity–stream function formulation, encapsulated in the system (44), (45), (47) and the density equation (42) leads at once to the spectral representation

$$\begin{aligned}
\psi(x, y, t) &= -\sum_{n=1}^{N}\sum_{m=1}^{M} V_{mn}(t)\sin\left(\frac{m\pi(y + h_1)}{h_2 + h_1}\right)\sin(nx),\\
\zeta(x, y, t) &= -\sum_{n=1}^{N}\sum_{m=1}^{M} \alpha_{mn} V_{mn}(t)\sin\left(\frac{m\pi(y + h_1)}{h_2 + h_1}\right)\sin(nx),
\end{aligned} \tag{48}$$

in which

$$\alpha_{mn} = n^2 + \left(\frac{m\pi}{h_2 + h_1}\right)^2. \tag{49}$$

These forms (48) satisfy the assumed slip boundary conditions (46), and velocity components u and v can be obtained at once by differentiation, according to (44). The perturbation density takes the spectral form

$$\bar{\rho}(x, y, t) = R_{00} - \sum_{m=1}^{M} R_{m0}(t) \sin\left(\frac{m\pi(y + h_1)}{h_2 + h_1}\right) - \sum_{n=1}^{N}\sum_{m=1}^{M} R_{mn}(t) \sin\left(\frac{m\pi(y + h_1)}{h_2 + h_1}\right) \cos(nx). \tag{50}$$

The vorticity equation (47) is decomposed spectrally, by multiplying by the basis functions

$$\sin\left(\frac{k\pi(y + h_1)}{h_2 + h_1}\right) \sin(\ell x) \quad k = 1, 2, \ldots, M, \quad \ell = 1, 2, \ldots, N \tag{51}$$

and integrating over the rectangle $-\pi < x < \pi$, $-h_1 < y < h_2$. After some algebra, this gives the system of equations

$$\frac{\mathrm{d}V_{k\ell}}{\mathrm{d}t} = \frac{\ell}{\alpha_{k\ell}} R_{k\ell}(t) - \beta\alpha_{k\ell} V_{k\ell}(t) + \frac{2}{\pi(h_2 + h_1)\alpha_{k\ell}} \int_{-\pi}^{\pi}\int_{-h_1}^{h_2} F(x, y, t) \sin\left(\frac{k\pi(y + h_1)}{h_2 + h_1}\right) \sin(\ell x)\, \mathrm{d}y\, \mathrm{d}x,$$
$$k = 1, 2, \ldots, M, \quad \ell = 1, 2, \ldots, N \tag{52}$$

involving the Fourier coefficients. The constants $\alpha_{k\ell}$ are as defined in (49), and the function in the integrand is defined for convenience to be

$$F(x, y, t) = u\frac{\partial\zeta}{\partial x} + v\frac{\partial\zeta}{\partial y}.$$

The density equation (42) is similarly decomposed, multiplying by basis functions similar to (51), but with the term $\sin(\ell x)$ replaced by $\cos(\ell x)$, and integrating over one period as above. This yields

$$\frac{\mathrm{d}R_{k0}}{\mathrm{d}t} = -\gamma\alpha_{k0} R_{k0}(t) + \frac{1}{\pi(h_2 + h_1)} \int_{-\pi}^{\pi}\int_{-h_1}^{h_2} G(x, y, t) \sin\left(\frac{k\pi(y + h_1)}{h_2 + h_1}\right) \mathrm{d}y\mathrm{d}x, \quad k = 1, 2, \ldots, M \tag{53}$$

for the zeroth-order terms in the index ℓ, and

$$\frac{\mathrm{d}R_{k\ell}}{\mathrm{d}t} = -\gamma\alpha_{k\ell} R_{k\ell}(t) + \frac{2}{\pi(h_2 + h_1)} \int_{-\pi}^{\pi}\int_{-h_1}^{h_2} G(x, y, t) \sin\left(\frac{k\pi(y + h_1)}{h_2 + h_1}\right) \cos(\ell x)\, \mathrm{d}y\, \mathrm{d}x,$$
$$k = 1, 2, \ldots, M, \ell = 1, 2, \ldots, N. \tag{54}$$

In these equations, it has been convenient to write

$$G(x, y, t) = u\frac{\partial\bar{\rho}}{\partial x} + v\frac{\partial\bar{\rho}}{\partial y}.$$

Equations (52–54) constitute a system of $M(1 + 2N)$ ordinary differential equations for the Fourier coefficients in the representations (48) and (50). The constant coefficient R_{00} is able to be calculated in terms of the pressure, but is not evaluated here since it plays only a minor role in the solution. This large system of differential equations is then solved using a fourth-order Runge–Kutta method to integrate the coefficients forward in time. An analysis of the Runge–Kutta technique shows it to be stable in the corresponding linearized viscous Boussinesq problem, and numerical experience with the technique indicates that it remains stable for the nonlinear problem, too.

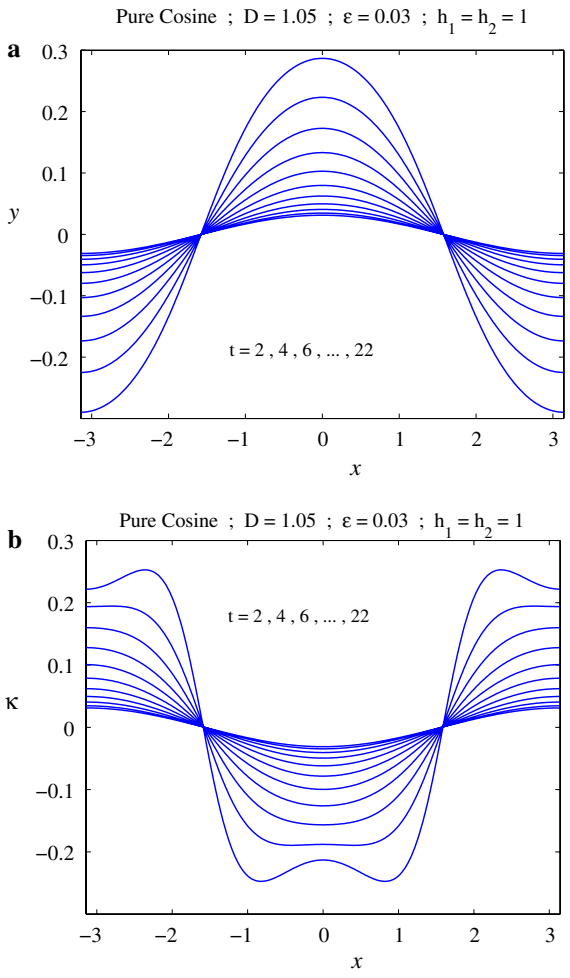

Fig. 2 (**a**) Interface profiles and (**b**) Interface curvatures, at a sequence of times as indicated, for a purely inviscid flow in finite-depth fluid, with wall positions given by parameters $h_1 = h_2 = 1$

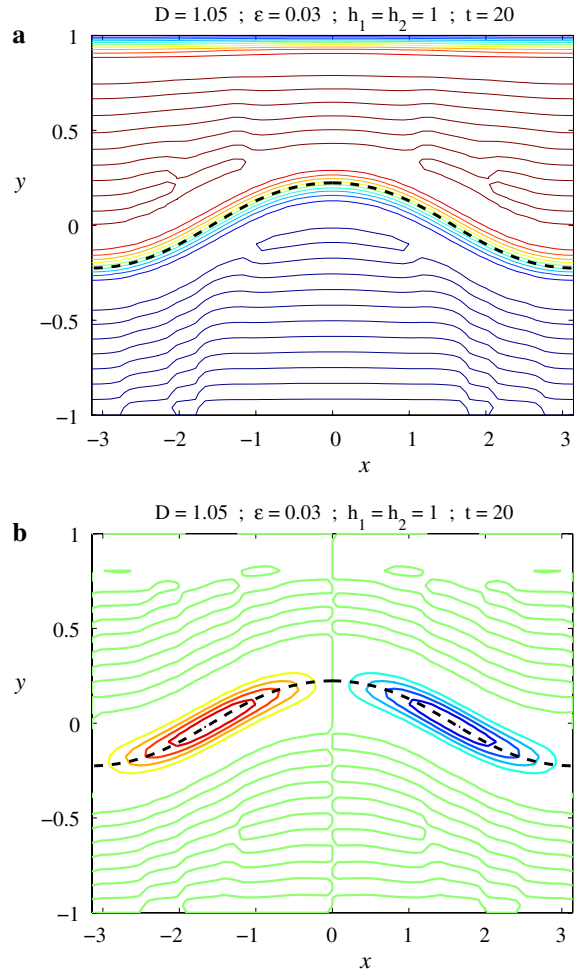

Fig. 3 A comparison of the inviscid and viscous solutions at time $t = 20$, for the solution illustrated in Fig. 2. In each diagram, the inviscid interface is shown with a *dashed line*, and is shown against (**a**) contours of the density and (**b**) contours of the vorticity, for the viscous solution. The vorticity in (**b**) is negligible except for those contours close to the interface, at which vorticity is positive for $x < 0$ and negative for $x > 0$

5 Presentation of results

In this section, we present a sample of the results of computation for inviscid and viscous fluids, using the models and algorithms presented in Sects. 2– 4. Attention is focussed in particular on the relationship between the purely inviscid behaviour and that of the solutions for which viscous effects have been included.

Figure 2(a) shows the evolution of the interface in a purely inviscid calculation, as illustrated by 11 profiles at different times $t = 2, 4, 6, \ldots, 22$. The density ratio is $D = 1.05$. The starting conditions at $t = 0$ were that the fluid was stationary, so that the coefficients P_n and Q_n were all zero in (40), and the initial interface profile was a pure cosine form $\eta(x, 0) = \epsilon \cos x$. This is accomplished by setting all the coefficients A_n and B_n in (16) to zero, with the exception of $B_1 = \epsilon$, which defines the wave amplitude. For this solution, $\epsilon = 0.03$.

It is clear from Fig. 2(a) that the wave profile essentially retains its initial cosine shape as it grows in amplitude. Nevertheless, the solution algorithm fails at a time slightly in excess of $t = 22$, since the numerical integration of the system of differential equations (36) is not capable of continuing much beyond that time. Thus the solution for $t = 22$ in Fig. 2(a) represents about the largest time for which inviscid solutions can be obtained for this case.

The explanation for the sudden failure of the numerical scheme at about $t = 22$ is found from a consideration of the curvature along the interface. For the classical Rayleigh–Taylor problem in infinite depth fluid, discussed in Sect. 2, Baker et al. [20] presented an asymptotic argument that, for initial sinusoidal disturbances of small amplitude, the curvature develops a singularity at the critical time

$$t_C = \sqrt{1/\mathcal{A}}\log(1/\epsilon), \tag{55}$$

in the non-dimensional variables of the present paper. The constant $\mathcal{A}$ is the Atwood number, defined in terms of the density ratio in (13). For the solution shown in Fig. 2, Eq. 55 indicates that the time at which a curvature singularity occurs is $t_C = 22.45$, and this is in good agreement with the present numerical results.

The development of the curvature at the interface for this same case is shown in Fig. 2(b). The curvature was computed using (31). For small times, the profile behaves approximately as $\kappa = -\epsilon\cos x$ as is to be expected, and this sinusoidal shape persists, approximately, over most of the times for which solutions can be computed. However, for the last profile at $t = 22$, large peaks begin to develop either side of the zeros in curvature at about $x = \pm\pi/2$, consistently with the analysis of Moore [8] and Baker et al. [20].

In Fig. 3, we present a comparison of the inviscid Rayleigh–Taylor solution with that obtained for the viscous Boussinesq fluid in Sect. 4. This is for the same case illustrated in Fig. 2, for a density ratio $D = 1.05$, an initial amplitude $\epsilon = 0.03$ and fluid depths $h_1 = h_2 = 1$. The viscosity and diffusion parameters were taken to be $\beta = \gamma = 10^{-4}$, and $M = N = 25$ Fourier coefficients were taken in each spatial variable. In each diagram, the inviscid interface, computed with the method of Sect. 3, has been shown as a thick dashed line.

The initial conditions for the viscous solution shown in Fig. 3 were that the fluid velocity started from zero. This is achieved simply by setting coefficients $V_{mn}(0) = 0$ in (48). In addition, the initial density profile has been chosen to conform as closely as possible to the pure cosine form of the interface for the inviscid solution shown in Fig. 2; this has been achieved by setting

$$\bar{\rho}(x, y, 0) = \text{constant} + \begin{cases} 0 & \text{for } -h_1 < y < \epsilon\cos x, \\ D-1 & \text{for } \epsilon\cos x < y < h_2. \end{cases} \tag{56}$$

This initial density is decomposed spectrally, by multiplying (56) by basis functions similar to (51), but with the term $\sin(\ell x)$ replaced by $\cos(\ell x)$, and integrating over the domain $-\pi < x < \pi$, $-h_1 < y < h_2$. After some calculation, this gives

$$\begin{aligned} R_{k0}(0) &= \frac{2(D-1)}{k\pi}\cos(k\pi)\left[1 - \cos\left(\frac{k\pi h_2}{h_2+h_1}\right)J_0\left(\frac{k\pi\epsilon}{h_2+h_1}\right)\right], \\ R_{k\ell}(0) &= -\frac{4(D-1)}{k\pi}J_\ell\left(\frac{k\pi\epsilon}{h_2+h_1}\right)\cos\left(\frac{k\pi h_1}{h_2+h_1} + \frac{\ell\pi}{2}\right). \end{aligned} \tag{57}$$

The functions J_0 and J_ℓ in (57) are first-kind Bessel functions of orders 0 and ℓ respectively, and were obtained using integral identities from [21, pp. 414, 415].

In Fig. 3(a), contours of the density $\bar{\rho}(x, y, t) - R_{00}$, computed using (50), are shown for the viscous solution. The high concentration of contour lines in the centre of the figure indicates the location of the effective interface, at which the density makes a smooth but rapid transition from one state to another; this is equivalent to the two distinct fluids in the purely inviscid case. There is very close agreement between the predictions of this viscous model and the location of the interface predicted by the inviscid equations.

Figure 3(b) shows the same inviscid interface, but now overlying contours of the vorticity ζ in (48). This function is anti-symmetric in x, and there is a contour $\zeta = 0$ down the y-axis, as expected. The most significant feature of this diagram, however, are the two elliptical contours of vorticity clustered at the location of the inviscid interface. These show a high concentration of vorticity at the interface in the viscous problem, and the largest absolute value

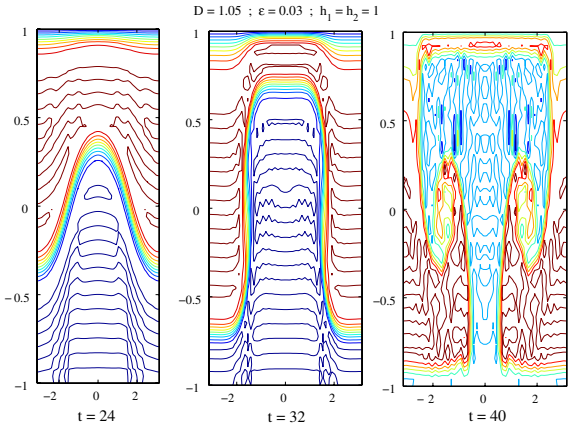

Fig. 4 Growth of the unstable solution for viscous fluid and the same case as illustrated in Figs. 2 and 3. Density contours for the solution are shown for the three times $t = 24$, 32 and 40 beyond the critical time at which the inviscid solution fails

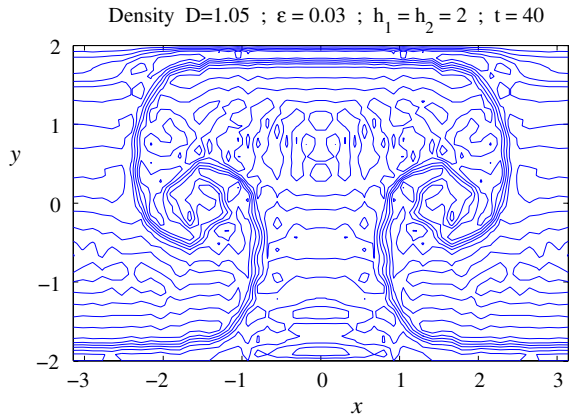

Fig. 5 A solution at time $t = 40$ for density ratio $D = 1.05$ and initial amplitude $\epsilon = 0.03$, and wall locations $h_1 = h_2 = 2$. The scales on the axes are equal, so that the solution is as it would appear

of vorticity occurs at precisely the two points at which the inviscid model seeks to develop singularities in the curvature. In summary, therefore, the inviscid and the viscous solutions agree very closely almost until the critical time (55) is attained; whereas the inviscid model then fails through the formation of curvature singularities at that time, viscosity although small, nevertheless prevents singular behaviour by the generation of large vorticity at those points. This confirms that the prediction of a curvature singularity in an inviscid model can be expected to trigger roll-up of the interface in a real fluid model in which viscosity is included.

Three viscous solutions for three times beyond the critical time in (55) are shown in Fig. 4. The first solution at $t = 24$ occurs slightly after the critical time $t_C = 22.45$, and still retains essentially the same cosine shape as all the inviscid interfaces shown in Fig. 2(a). By time $t = 32$, however, slight over-hanging portions in the interface have appeared, and the wave now takes on an elongated squarer shape. Evidently the upper wall at $y = h_2 = 1$ is having an influence on the development of this unstable flow. At time $t = 40$, a fully developed plume has evolved in the fluid, consistently with the results that Tryggvason [22] computed using Lagrangian–Eulerian finite-difference schemes. There are over-hanging spiral portions on the interface, and the heavier upper fluid is entrained into them.

A more detailed view of the plume at time $t = 40$ is given in Fig. 5, for the same density ratio $D = 1.05$ and initial cosine amplitude $\epsilon = 0.03$. In this profile, however, the upper and lower horizontal walls are moved further out to locations $h_1 = h_2 = 2$, to reduce the influence of the walls on the evolving unstable solution. Nevertheless, the plume has a rather similar overall shape to that shown in Fig. 4 at $t = 40$. There are spiral-shaped over-hanging portions, and there is a long flat portion at the top of the plume, reflecting the effect of the upper wall at $y = h_2 = 2$.

As a comparison, a further solution is presented in Fig. 6, for the same case $D = 1.05$ and $\epsilon = 0.03$, but now with asymmetrically positioned walls. The lower wall is at $y = -h_1 = -2$ as in Fig. 5, but the upper wall is further away, at height $y = h_2 = 4$. It is evident from Fig. 6 that the influence of the upper wall has been greatly reduced, since now the top of the rising plume is quite rounded in shape. The spiral over-hanging portions are still present in the profile, however. For these solutions, there is again good agreement between the purely inviscid solution and the viscous results in the earlier stages of the flow, as with Fig. 3, although these results are not shown here.

A further solution is shown in Fig. 7 at time $t = 40$, for the case $D = 1.05$ and wall locations $h_1 = h_2 = 2$ as in Fig. 5. Here, however, the initial disturbance to the interface has the opposite sign $\epsilon = -0.03$ to that in Fig. 5, and as a result, the growth of the plume is apparently downwards instead of being directed upwards as before. It turns out, however, that the orientation of the plume is of little significance, due to the periodicity of the solution in the x-coordinate. In fact, the result in Fig. 7 is really the same as in Fig. 5, but translated by π units along the x-axis.

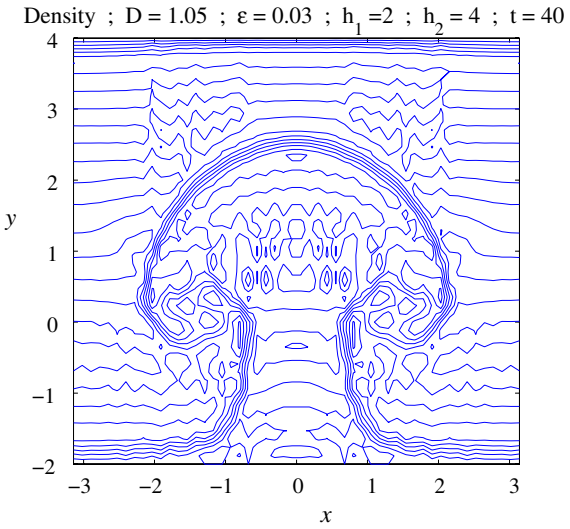

Fig. 6 Density contours for a solution at time $t = 40$, for density ratio $D = 1.05$ and initial amplitude $\epsilon = 0.03$, and asymmetrical wall locations $h_1 = 2$ and $h_2 = 4$. The scales on the axes are equal, so that the solution is as it would appear

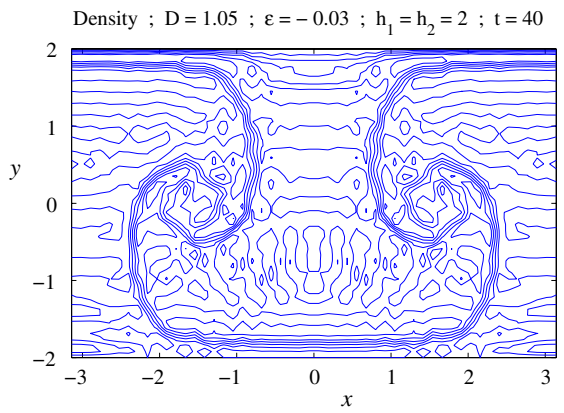

Fig. 7 A solution at time $t = 40$ for density ratio $D = 1.05$ and initial amplitude $\epsilon = -0.03$, and wall locations $h_1 = h_2 = 2$. The scales on the axes are equal, so that the solution is as it would appear

The form of the initial profile can have a strong influence on how the Rayleigh–Taylor instability develops for subsequent times, as is to be expected. In fact, Forbes et al. [15] showed that they could produce weakly over-hanging portions in the interface, even for the inviscid problem, by starting from a slightly distorted sinusoidal profile. Similar effects have been produced with their choice of initial conditions in this present work also, although that will not be discussed further here. Instead, we consider here the periodic partial cosine profile

$$H(x,0) = \begin{cases} \epsilon\cos(x/q) & \text{for } 0 < x < q\pi, \\ -\epsilon & \text{for } q\pi < x < \pi. \end{cases} \tag{58}$$

In this expression, the constant q takes values in the interval $0 < q < 1$. This function (58) and its first derivative are continuous, although the second derivative is discontinuous at the points $x = \pm q\pi$.

For the inviscid solutions, in which the interface is represented parametrically in terms of the scaled arclength ξ, this initial condition (58) may be achieved by setting all coefficients $A_n(0) = 0$ in (16), along with $B_0(0) = -\epsilon(1-q)$ and

$$B_n(0) = \frac{2\epsilon\sin(nq\pi)}{n\pi(1+qn)(1-qn)} \quad \text{if } q \neq 1/n,$$
$$B_n(0) = \epsilon/n \quad \text{if } q = 1/n.$$

Figure 8(a) shows a sequence of eleven interface profiles, for the classical Rayleigh–Taylor problem of Sect. 2 with zero fluid acceleration ($\alpha = 0$), and starting from the partial-cosine initial profile. The amplitude at $t = 0$ was $\epsilon = 0.03$ and the width parameter q in (58) was set to $q = 0.3$. The density ratio is $D = 1.05$, as in previously displayed solutions. It is evident that the interface develops an upward moving section in the centre, but two downwardly directed portions either side. Although the profile remains smooth, it nevertheless develops reasonably steep portions, particularly near the points where the interface crosses over the x-axis. The numerical method of Sect. 2 fails at a slightly later time than $t = 11$, and so this last profile in Fig. 8(a) represents about the largest time for which solutions can be computed in this case.

Interface curvatures have again been computed for this example, using (31), and are shown in Fig. 8(b), for ten different times. The result for $t = 11$ is not shown, since the curvature at this time contains very large values and is subject to error. In particular, numerical oscillations are generated by the large and nearly discontinuous

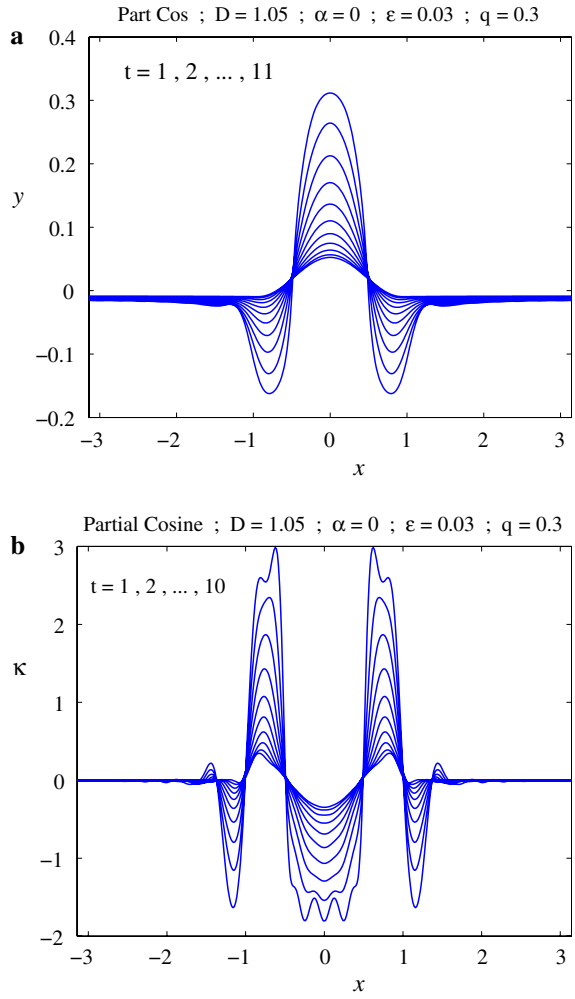

Fig. 8 (**a**) Interface profiles and (**b**) interface curvatures, at a sequence of times as indicated, for a purely inviscid flow in infinitely deep fluid. The initial interface had the shape of a partial-cosine profile, with $q = 0.3$

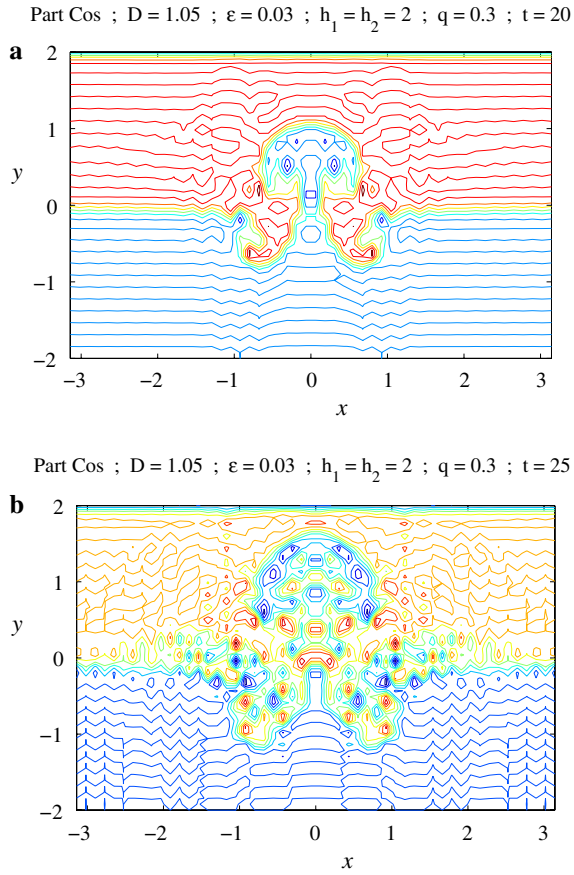

Fig. 9 Viscous solutions for (**a**) time $t = 20$ and (**b**) time $t = 25$. Density contours are shown for a partial-cosine initial profile, with $q = 0.3$. The scales on the axes are equal, so that the solutions are as they would actually appear

curvatures, giving rise to a type of Gibbs' phenomenon (see, for example, [23, p. 510]). In fact, some evidence of these oscillatory errors can be seen in the curvature at time $t = 10$. Nevertheless, Fig. 8(b) clearly indicates that curvatures become very large at selected points along the interface, and singularities are likely to be formed at these points at a time slightly later than $t = 11$. Very large values of curvature are created essentially at the four points either side of the upward and downward lobes in the wave profile. From the results shown in Fig. 3(b), it is to be expected that, in the corresponding viscous problem, large values of vorticity will form near these four points, and that interface roll-up is likely there.

This prediction is confirmed in the results presented in Fig. 9. Here, the viscous Boussinesq model of Sect. 4 has been run for the same case $D = 1.05$ as for Fig. 8, and with the same partial-cosine initial profile of amplitude $\epsilon = 0.3$ and width parameter $q = 0.3$. This has been achieved by setting coefficients $V_{mn}(0) = 0$ in (48). The coefficients at $t = 0$ in the density profile (50) are obtained directly from the relations

$$R_{k0}(0) = -\frac{1}{\pi(h_2+h_1)} \int_{-\pi}^{\pi} \int_{-h_1}^{h_2} \bar{\rho}(x, y, 0) \sin\left(\frac{k\pi(y+h_1)}{h_2+h_1}\right) \mathrm{d}y\, \mathrm{d}x, \quad k = 1, 2, \ldots, M$$

and

$$R_{k\ell}(0) = -\frac{2}{\pi(h_2+h_1)} \int_{-\pi}^{\pi} \int_{-h_1}^{h_2} \bar{\rho}(x, y, 0) \sin\left(\frac{k\pi(y+h_1)}{h_2+h_1}\right) \cos(\ell x)\, \mathrm{d}y\, \mathrm{d}x, \quad k{=}1, 2, \ldots, M, \quad \ell{=}1, 2, \ldots, N.$$

The initial perturbation density profile $\bar{\rho}(x, y, 0)$ in these expressions is taken to be $(D-1)$ above the line in (58) and zero below it. The integrals in y are evaluated in closed form, but the x-integrals are evaluated numerically. As these integrands are no longer periodic, high accuracy can not be guaranteed using the simple trapezoidal rule, and instead, we use Gauss–Legendre quadrature with 101 grid points. The abscissae and weights for this process have been computed using the algorithm written by Greg von Winckel, and made available on the MATLAB file exchange site [24].

Figure 9(a) shows a solution at time $t = 20$, for Rayleigh–Taylor instability in a viscous Boussinesq fluid started with the partial-cosine interface profile (58) with $q = 0.3$. As expected from Fig. 8(b), there are four points along the interface at which regions of high vorticity form, causing roll-up to occur. Two of these are located in the downwardly directed jets, which have clearly begun to curl outwards in Fig. 9(a). The other two regions of high vorticity occur either side of the upwardly directed plume, which as a result has developed overhanging sections.

An interesting phenomenon occurs in this example, as time increases and the instability develops. This is illustrated in Fig. 9(b) at time $t = 25$. The upwardly directed plume has now detached from the lower fluid altogether, forming a separate umbrella structure that continues to move upward toward the top wall. For this particular initial condition, there is evidently strong mixing of the two fluids at reasonably early times.

6 Discussion and conclusions

This paper has studied in detail the development of the Rayleigh–Taylor instability, both for inviscid and viscous fluids. A novel spectral method developed by Forbes et al. [15] has been adapted to track the movement of the interface between two inviscid fluids. It allows the curvature along the interface to be computed accurately, which is a feature not shared with many other numerical techniques. The results show the development of regions of very high curvature at certain points on the interface, heralding the formation of genuine curvature singularities at these points. When a purely sinusoidal initial profile of small amplitude is chosen, the time at which the singularity forms agrees closely with the asymptotic estimate (55) of Baker et al. [20]. This has been found to be the case for values of density ratio D other than those presented in this paper, provided that the initial amplitude ϵ is sufficiently small.

The acceleration α of the fluids in the classical Rayleigh–Taylor problem has been shown here not to have a significant effect on the actual development of the instability, and this suggests the further study of the instability in a stationary fluid system of finite depth. This same problem has been solved here also, for a viscous Boussinesq fluid with continuous stratification except at the first instant when it is allowed to have a density discontinuity at an effective interface; this can be accommodated in the present scheme which is based on a spectral method for this viscous system.

It has been shown here that the viscous and inviscid solutions agree extremely closely for the early stages of the flow, until the curvature singularity forms at the interface, in the inviscid problem. A close comparison with the viscous solution at that time shows that viscosity prevents the curvature singularity forming, by creating regions of high vorticity at precisely those same points. This is not possible for purely inviscid flow, since no mechanism exists there for vorticity creation, as a consequence of Kelvin's circulation theorem (see [18, p. 273]); thus the motion remains irrotational in the inviscid model for any flow started from rest. This then confirms that the singularity formation in the purely inviscid flow is the trigger for interface roll-up when viscosity is taken into account.

The initial conditions have a very strong influence on the subsequent development of the flow, which is to be expected, since it is unstable and grows with time. Several different starting shapes have been investigated during the course of this study, and we have shown here the particular instance of a partial-cosine profile, repeated periodically along the x-axis. In this case, an upwardly moving plume of the lighter lower fluid forms as usual, but for this initial condition, the top of the plume then detaches and continues to move upward as a separate bubble. Increasing the density ratio D does not appear to change these basic features of the flow, but does cause these extreme effects to occur at earlier times.

References

1. Lord Rayleigh (1883) Investigation of the character of the equilibrium of an incompressible heavy fluid of variable density. Proc Lond Math Soc 14:170–177
2. Sir Taylor GI (1950) The instability of liquid surfaces when accelerated in a direction perpendicular to their planes, I. Proc R Soc Lond A 201:192–196
3. Sharp DH (1984) An overview of Rayleigh-Taylor instability. Physica D 12:3–18
4. Kull HJ (1991) Theory of the Rayleigh-Taylor instability. Phys Lett 206:197–325
5. Inogamov NA (1999) The role of Rayleigh-Taylor and Richtmyer-Meshkov instabilities in astrophysics: an introduction. Astrophys Space Phys 10:1–335
6. Lazier J, Pickart R, Rhines P (2001) Deep convection. In: Siedler G, Church J, Gould J (eds) Ocean circulation and climate: observing and modelling the global ocean, vol 77 in international geophysics series. Academic Press, San Diego pp 387–400
7. McClure-Griffiths NM, Dickey JM, Gaensler BM, Green AJ (2003) Loops, drips, and walls in the galactic chimney GSH 277+00+36. Astrophys J 594:833–843
8. Moore DW (1979) The spontaneous appearance of a singularity in the shape of an evolving vortex sheet. Proc R Soc. Lond A 365:105–119
9. Cowley SJ, Baker GR, Tanveer S (1999) On the formation of Moore curvature singularities in vortex sheets. J Fluid Mech 378: 233–267
10. Krasny R (1986) Desingularization of periodic vortex sheet roll-up. J Comput Phys 65:292–313
11. Baker GR, Pham LD (2006) A comparison of blob-methods for vortex sheet roll-up. J Fluid Mech 547:297–316
12. Tryggvason G, Dahm WJA, Sbeih K (1991) Fine structure of vortex sheet rollup by viscous and inviscid simulation. J Fluids Eng 113:31–36
13. Tryggvason G, Unverdi SO (1990) Computations of three-dimensional Rayleigh-Taylor instability. Phys Fluids A 2:656–659
14. Stone JM, Gardiner T (2007) Nonlinear evolution of the magnetohydrodynamic Rayleigh-Taylor instability. Phys Fluids 19, 094104:19
15. Forbes LK, Chen MJ, Trenham CE (2007) Computing unstable periodic waves at the interface of two inviscid fluids in uniform vertical flow. J Comput Phys 221:269–287
16. Forbes LK, Hocking GC (2007) Unsteady draining flows from a rectangular tank. Phys Fluids 19, 082104:14
17. Farrow DE, Hocking GC (2006) A numerical model for withdrawal from a two-layer fluid. J Fluid Mech 549:141–157
18. Batchelor GK (1967) An introduction to fluid dynamics. Cambridge University Press, Cambridge
19. Atkinson KA (1978) An introduction to numerical analysis. Wiley, New York
20. Baker G, Caflisch RE, Siegel M (1993) Singularity formation during Rayleigh-Taylor instability. J Fluid Mech 252:51–78
21. Gradshteyn IS, Ryzhik IM (2000) Tables of integrals, series and products, 6th edn. Academic Press, San Diego
22. Tryggvason G (1988) Numerical simulations of the Rayleigh-Taylor instability. J Comput Phys 75:253–282
23. Kreyszig E (2006) Advanced engineering mathematics, 9th edn. Wiley, New York
24. von Winckel G, lgwt.m, at: MATLAB file exchange website, written (2004) http://www.mathworks.com/matlabcentral/fileexchange/loadFile.do?objectId=4540&objectType=file